ISSN 1674-1056
http://cpb.iphy.ac.cn
http://iopscience.iop.org/cpb
中国物理 B
Chinese Physics
中国物理
Chinese Physics B

Photovoltaic effects in reconfigurable heterostructured black phosphorus transistors

Siqi Hu(胡思奇), Ruijuan Tian(田睿娟), Xiaoguang Luo(罗小光), Rui Yin(殷瑞), Yingchun Cheng(程迎春), Jianlin Zhao(赵建林), Xiaomu Wang(王肖沐), Xuetao Gan(甘雪涛)

Citation: Chin. Phys. B . 2018, 27(12): 128502. **doi:** 10.1088/1674-1056/27/12/128502
Journal homepage: http://cpb.iphy.ac.cn; http://iopscience.iop.org/cpb

What follows is a list of articles you may be interested in

Improved performance of Ge n^+/p diode by combining laser annealing and epitaxial Si passivation

Chen Wang(王尘), Yihong Xu(许怡红), Cheng Li(李成), Haijun Lin(林海军)

Chin. Phys. B . 2018, 27(1): 018502. **doi:** 10.1088/1674-1056/27/1/018502

Impact of Al addition on the formation of Ni germanosilicide layers under different temperature annealing

Xiao-Ran Meng(孟骁然), Yun-Xia Ping(平云霞), Wen-Jie Yu(俞文杰), Zhong-Ying Xue(薛忠营), Xing Wei(魏星), Miao Zhang(张苗), Zeng-Feng Di(狄增峰), Bo Zhang(张波), Qing-Tai Zhao(赵清太)

Chin. Phys. B . 2017, 26(9): 098503. **doi:** 10.1088/1674-1056/26/9/098503

Photoemission cross section: A critical parameter in the impurity photovoltaic effect

Jiren Yuan(袁吉仁), Haibin Huang(黄海宾), Xinhua Deng(邓新华), Zhihao Yue(岳之浩), Yuping He(何玉平), Naigen Zhou(周耐根), Lang Zhou(周浪)

Chin. Phys. B . 2017, 26(1): 018503. **doi:** 10.1088/1674-1056/26/1/018503

Enhanced near-infrared responsivity of silicon photodetector by the impurity photovoltaic effect

Yuan Ji-Ren, Huang Hai-Bin, Deng Xin-Hua, Liang Xiao-Jun, Zhou Nai-Gen, Zhou Lang

Chin. Phys. B . 2015, 24(4): 048501. **doi:** 10.1088/1674-1056/24/4/048501

A novel integrated ultraviolet photodetector based on standard CMOS process

Wang Han, Jin Xiang-Liang, Chen Chang-Ping, Tian Man-Fang, Zhu Ke-Han

Chin. Phys. B . 2015, 24(3): 038501. **doi:** 10.1088/1674-1056/24/3/038501

SPECIAL TOPIC — Photodetector: Materials, physics, and applications

Photovoltaic effects in reconfigurable heterostructured black phosphorus transistors*

Siqi Hu(胡思奇)[1], Ruijuan Tian(田睿娟)[1], Xiaoguang Luo(罗小光)[2], Rui Yin(殷瑞)[1], Yingchun Cheng(程迎春)[2], Jianlin Zhao(赵建林)[1], Xiaomu Wang(王肖沐)[3], and Xuetao Gan(甘雪涛)[1,†]

[1] *MOE Key Laboratory of Material Physics and Chemistry under Extraordinary Conditions, and Shaanxi Key Laboratory of Optical Information Technology, School of Science, Northwestern Polytechnical Univeristy, Xi'an* 710072, *China*

[2] *Shannxi Institute of Flexible Electronics, Northwestern Polytechnical University, Xi'an* 710072, *China*

[3] *School of Electronic Science and Engineering, Nanjing University, Nanjing* 210023, *China*

(Received 20 September 2018; revised manuscript received 30 September 2018; published online 25 November 2018)

We demonstrate a reconfigurable black phosphorus electrical field transistor, which is van der Waals heterostructured with few-layer graphene and hexagonal boron nitride flakes. Varied homojunctions could be realized by controlling both source–drain and top-gate voltages. With the spatially resolved scanning photocurrent microscopy technique, photovoltaic photocurrents originated from the band-bending regions are observed, confirming nine different configurations for each set of fixed voltages. In addition, as a phototransistor, high responsivity (∼ 800 mA/W) and fast response speed (∼ 230 μs) are obtained from the device. The reconfigurable van der Waals heterostructured transistors may offer a promising structure towards electrically tunable black phosphorus-based optoelectronic devices.

Keywords: black phosphorus, reconfigurable heterostructure, photovoltaic effect, photocurrent

PACS: 85.30.Kk, 85.60.Bt, 85.60.Dw **DOI:** 10.1088/1674-1056/27/12/128502

1. Introduction

Two-dimensional (2D) materials rose sharply after the exfoliation of graphene in 2004.[1–3] A large number of 2D materials ranging from semimetal to semiconductor and to insulator have been investigated,[4–6] and some of them are considered as promising next-generation constituents in optoelectronic circuitry.[7–9] Graphene was once a good choice for optoelectronic applications due to the broad band absorption and high carrier mobility (in the order of 10^4 $cm^2 \cdot V^{-1} \cdot s$-1). However, the absence of bandgap makes graphene only a good 2D electrode due to the low absorbance and bad current on/off ratio. For a single device such as a field-effect transistor (FET), the high mobility channel materials with moderate bandgap are desired.

Black phosphorus (BP) with a monolayer thickness of ∼ 0.53 nm recently emerges as a good candidate for 2D material-based optoelectronics.[10] Its direct bandgap could be varied from 0.3 eV to 1.3 eV by reducing the layer number to monolayer gradually.[11] This bandgap leads to a very good current on/off ratios (up to 10^5) in the FET, which is superior to the gapless graphene. The carrier mobility of few-layer BP, in the order of 10^2 $cm^2 \cdot V^{-1} \cdot s^{-1}$ at room temperature,[12] is higher than those in most of the 2D semiconductors, such as transition-metal dichalcogenides. In addition, BP's ambipolarity promises it to be a good channel material for constructing electrostatically tuned optoelectronic devices.[11–17] The limitation for BP devices is mainly the bad air-stability, which fortunately could be overcome from encapsulation by other transparent insulators.[18] Hexagonal boron nitride (h-BN) is such a 2D insulator with a large bandgap (> 5 eV), which is also suitable as a gate dielectric material.[4,6,19] Combining 2D materials with different electronic properties ranging from semimetal (*e.g.*, graphene) to semiconducting (*e.g.*, BP) and to insulating (*e.g.*, h-BN), one could fabricate various electronic and optoelectronic devices by simple van der Waals contact with flat surfaces and disorder-free interfaces.

Here, we present the achievement of a reconfigurable BP FET, which is van der Waals heterostructured with graphene and h-BN. A few-layer BP channel is in contact with source-drain graphene electrodes and covered by a top h-BN dielectric layer. Another graphene sheet on the top of h-BN acts as the top-gate electrode. Nine different configurations of the homojunction over the BP channel are achieved by controlling both the drain-source voltages and gate voltages. The applied voltages are less than 2 V. All configurations can be spatially visualized and confirmed by scanning photocurrent microscopy (SPCM). Meanwhile, the phototransistor has a high responsivity (up to 800 mA/W) and a fast response speed (∼ 230 μs), offering potential applications towards photodetection and en-

*Project supported by the National Key Research and Development Program of China (Grant Nos. 2018YFA0307200 and 2017YFA0303800), the National Natural Science Foundations of China (Grant Nos. 61522507 and 61775183), the Key Research and Development Program in Shaanxi Province of China (Grant No. 2017KJXX-12), and the Fundamental Research Funds for the Central Universities (Grant Nos. 3102017jc01001 and 3102018jcc034).

†Corresponding author. E-mail: xuetaogan@nwpu.edu.cn

© 2018 Chinese Physical Society and IOP Publishing Ltd

ergy harvesting based on few-layer BP.

2. Fabrication and characterization of BP devices

Figure 1(a) shows the cross-section schematics of a BP-based top-gate FET on an SiO_2/Si substrate. Two prepatterned graphene sheets underneath the BP flake act as source and drain electrodes, sandwiched by two transferred h-BN flakes which perform as a substrate and a top-gate dielectric, respectively. The double-deck h-BN flakes also encapsulate BP flake to refrain it from degeneration. Another prepatterned graphene sheet was finally stamped above the BP channel region as the top-gate. To fabricate the device, graphene, BP and h-BN layers are mechanically cleaved from their bulk materials onto polydimethylsiloxane (PDMS) stamps,[20] which facilitates the precise alignment and transfer of the 2D flakes into the proposed heterostructures. An optical microscopic image of the finished device is shown in Fig. 1(b). To confirm the quality of the BP layer, Raman spectra are acquired from the device with the excitation of 532-nm laser. As shown in Fig. 1(c), characteristic A_g^1, B_{2g}, and A_g^2 peaks are clearly observed at the wave-number of 363.3 cm^{-1}, 440.4 cm^{-1}, and 469.2 cm^{-1}. Atomic force microscopy (AFM) technique is employed to examine the thicknesses of the 2D flakes. Figure 1(d) shows the AFM image of the area denoted by the black dashed box of Fig. 1(b), indicating thicknesses of BP and top h-BN are about 8 nm (15 layers) and 12 nm, respectively.

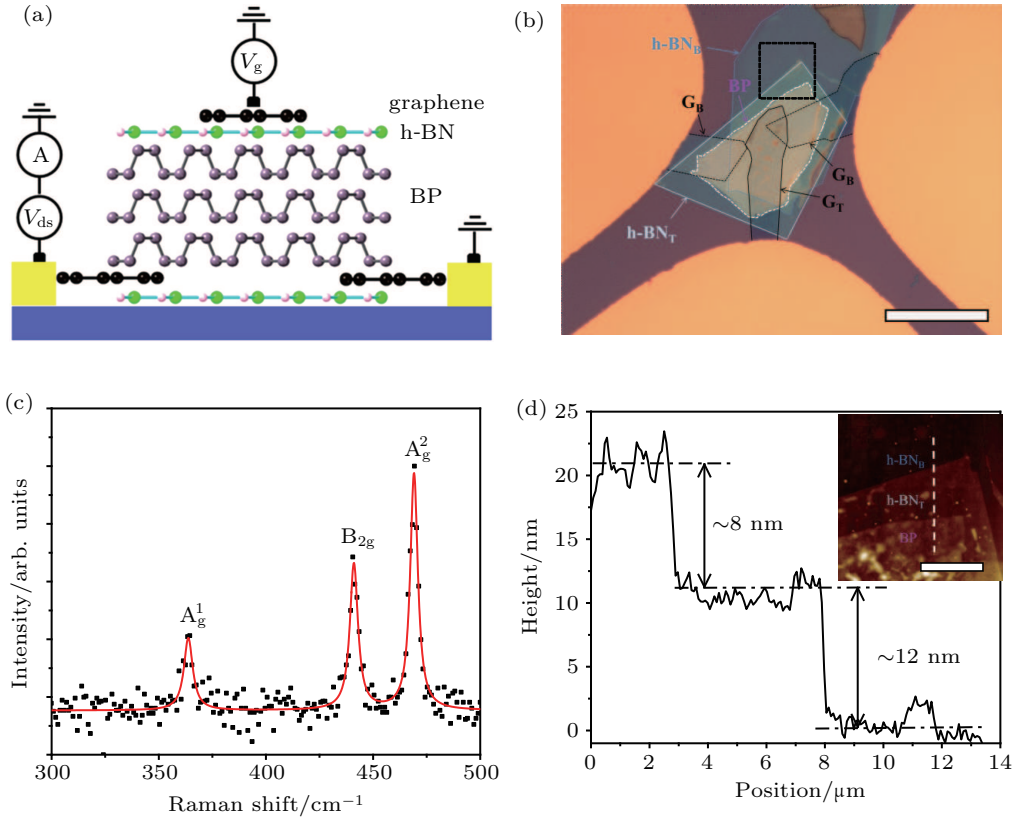


Fig. 1. (color online) BP FET based on van der Waals heterojunctions. (a) Cross-section schematics of a BP FET with all 2D constituents on SiO_2/Si substrate. The three-terminal measurement scheme is also shown. (b) Optical image of the device. The scale bar is 20 μm. (c) Raman spectra of BP flakes. (d) Atomic force microscopy image of the BP FET inside the dotted black box shown in panel (b). BP thickness is 8 nm and h-BN_T thickness is 12 nm. The scale bar is 5 μm.

3. Results and discussion

3.1. Reconfigurable operation of BP devices

A typical electrical transfer characteristic of the fabricated BP top-gate transistor is shown in Fig. 2(a), where the source-drain voltage is $V_{ds} = 10$ mV. A transport gap of $\Delta V_g \sim 0.38$ V is observed around $V_g = 0$ V, which is extracted from the linear extrapolation of I_{ds}. Subsequently, the band gap of BP can be estimated by the change of Fermi level (or chemical potential) E_F upon the transport gap,[21]

$$\Delta E_F = e\Delta V_g - \Delta\phi = e\Delta V_g - (e^2 n)/C_G, \quad (1)$$

where $\Delta\phi = e^2 n/C_G$ counts the variation in the electrostatic potential with the electron charge e, the carrier density n and the geometrical capacitance C_G. The carrier density in BP film can be estimated as $n = (\Delta V_g C_G)/e$ and the geometrical capacitance of top h-BN is $C_G = (\varepsilon_{h-BN})/h_{h-BN}$, with $\varepsilon_{h-BN} = 4.2\varepsilon$ (vacuum permittivity ε) the relative dielectric constant[4] of top h-BN and the thickness $h_{h-BN} = 12$ nm, respectively. We

then estimate that $C_G = 309.8$ nF/cm^{-2} and the band gap of the 15 layers BP film is $\Delta E_F = 0.32$ eV, which is close to the bulk band gap of ~ 0.3 eV.[22] It is known that the values of the electron affinity and the ionization potential relative to the vacuum of few-layer BP film are about 4.1 eV and 4.4 eV,[23] respectively, and thus the graphene Fermi energy (4.5 eV) is 0.1 eV lower than the top of the valence band of BP film from the band alignment. As a result, the band in BP film bends downward to the bottom graphene layer with a build-in field, and the device is intrinsic with slight p-type carriers. This is confirmed from the asymmetric transfer I_{ds}–V_g curve around $V_g = 0$ V, as shown in Fig. 2(a).

Figure 2(b) shows the output characteristics in semi-log and linear (inset) scales for V_g from -2 V to 2 V in the step of 1 V. The diode-like current rectifications were observed for all V_g's except that around 0 V. The V_g-dependent rectification behaviors could be modulated from the rectification directionalities, the polarities, and their degrees. For example, a positive forward current flows at positive V_{ds} when $V_g = -1$ V, while the direction of current is reversed when $V_g = 1$ V. From the electrical transfer characteristics ($|I_{ds}|$–V_g curves) versus different V_{ds} shown in Figs. 2(c) and 2(d), the ambipolarity at low V_{ds} is modulated to electron- or hole-dominant polarity as V_{ds} increases from -2 V to 2 V. Minimum subthreshold swing $S = dV_g/(d \ln I_{ds}) \sim 340$ mV/dec is observed at low source-drain voltage $|V_{ds}| = 0.1$ V. Besides, the measured Schottky barrier height between gold electrode and graphene (not shown here) is much smaller than that in the graphene-BP junction in our devices, thus we eliminate the influence of the Schottky junction. So far, tunable diode characteristics or polarities have been achieved in our device by adjusting V_{ds} and V_g, which are in the same voltage scale. In other words, our device can be reconfigured by a specified set of V_{ds} and V_g values.

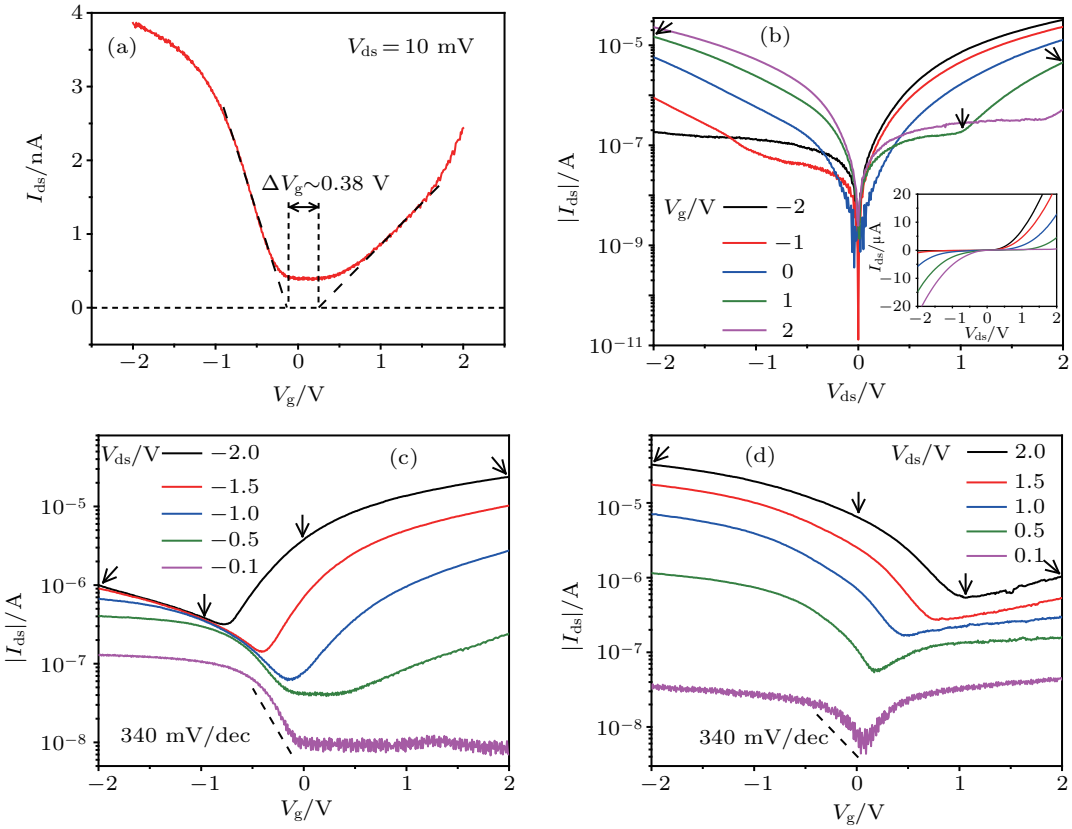


Fig. 2. (color online) Characteristics of the BP FET. (a) Electrical transfer characteristic (I_{ds}–V_g curve) at $V_{ds} = 10$ mV. (b) Semi-log plots of output characteristics ($|I_{ds}|$–V_{ds} curves) at various V_g values from -2 V to 2 V with a 1-V step. Inset: the corresponding linear plots. (c) and (d) Semi-log plots of electrical transfer characteristics for (c) negative and (d) positive V_{ds}.

The asymmetric property of Fig. 2(a) also implies the slight band bending at $V_g = 0$ V and $V_{ds} = 0$ V, where the Fermi energy is estimated to be a little lower than the mid-gap of BP film. Considering the weak photoresponse at low applied voltages from our following experimental results, we still regard this slight p-type as *i* (intrinsic) type. Figure 3 shows the band diagram configurations for each set of V_{ds} and V_g, corresponding to those arrows in the device characteristics of Figs. 2(b), 2(c), and 2(d). The equilibrium state when $V_g = 0$ V and $V_{ds} = 0$ V is shown in Fig. 3(a), which is regarded as an overall *i* type due to the nearly flat band configuration. To distinguish the reconfigurations of the device, the sign and magnitude of $V_{g,eff}(x) = V_g - V(x)$ are adopted to determine the carrier type (n type, i type, or p type) and carrier density, which is the effective gate field along the channel and $V(x)$ is the channel voltage. For the green curve of Fig. 2(b), when V_{ds}

varies from −2 V to 1 V and to 2 V at the fixed $V_g = 1$ V, the corresponding channel voltage along the channel (from left to right) can be expressed as [−2 V, 0 V], [1 V, 0 V], and [2 V, 0 V] respectively after assuming a constant voltage drop along the channel for simplicity. Then one can find the corresponding effective gate field as [3 V, 1 V], [0 V, 1 V], and [−1 V, 1 V], leading to n type, i–n type, and p–i–n type configurations, as shown in turn in Figs. 3(b)–3(d). The energy barriers formed at the contacts are asymmetric in these reconfigurations, resulting in asymmetric injection of dominant carriers, and finally realizing channel conductance. In the same way, when V_g varies from −2 V to −1 V, 0 V, and 2 V at the fixed $V_{ds} = -2$ V (*i.e.*, the arrows in the black curve of Fig. 2(c)), the corresponding band structures can be assigned to i–p, n–i–p, n–i, and n, respectively, as shown in turn in Figs. 3(e)–3(h). At the fixed $V_{ds} = 2$ V, V_g varies from −2 V to 0 V, 1 V, and 2 V (*i.e.*, the arrows in the black curve of Fig. 2(d)) corresponds to p, p–i, p–i–n, and i–n, respectively, as shown in turn in Figs. 3(i)–3(l). Therefore, nine different configurations (Fig. 3) from a single device can be achieved for each set of V_{ds} and V_g, which will be confirmed by the spatially resolved SPCM technique in the following.

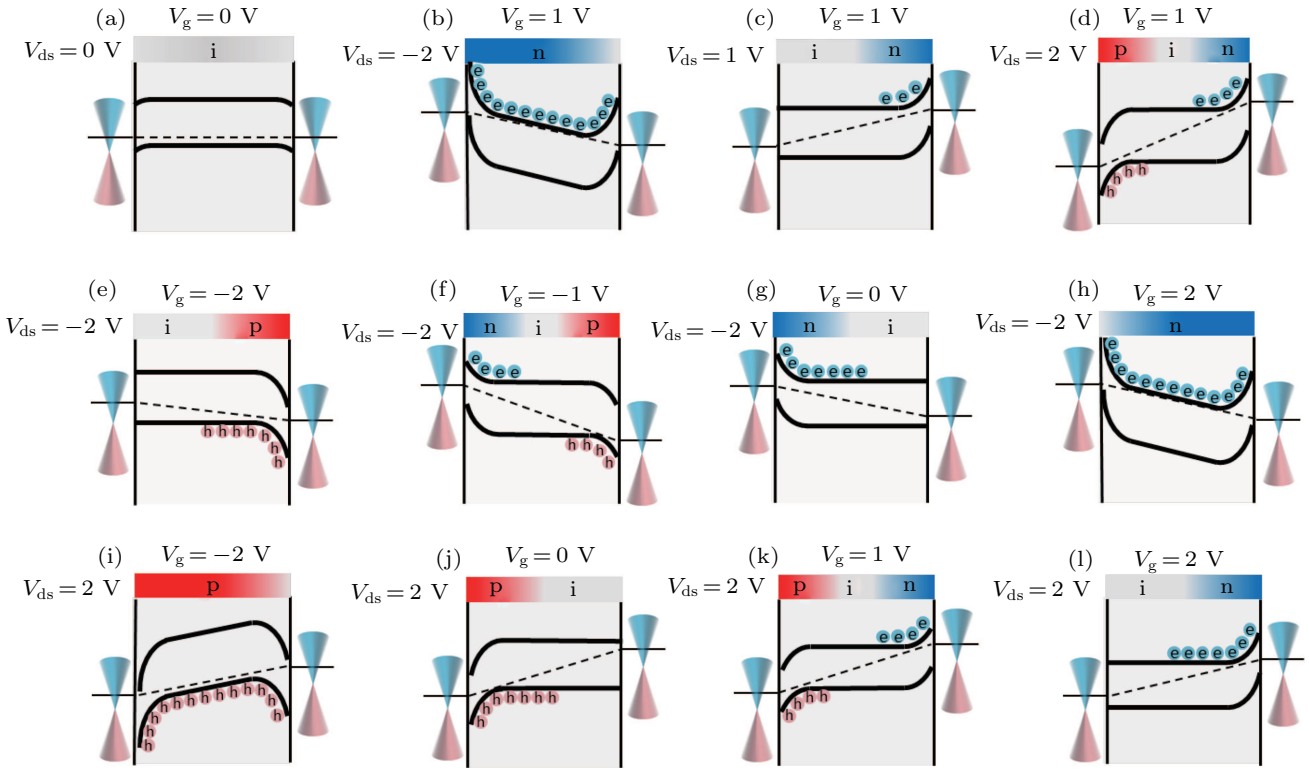


Fig. 3. (color online) Band diagrams for reconfigurable device operations. (a) Schematic band diagram of a BP FET with all 2D components at equilibrium ($V_{ds} = V_g = 0$ V). (b)–(d) Band configurations for the $|I_{ds}|$–V_{ds} characteristic, following the arrows in the green curve shown in Fig. 2(b). (e)–(h) Band configurations for the $|I_{ds}|$–V_g characteristics following the arrows in the black curve shown in Fig. 2(c). (i)–(l) Band configurations for the $|I_{ds}|$–V_g characteristics following the arrows in the black curve shown in Fig. 2(d).

3.2. Photovoltaic effect in reconfigurable heterostructured BP devices

In the fabricated heterostructued BP device, photocurrent would generate at the band bending region via the photovoltaic effect. The spatially resolved SPCM technique is therefore a good way to visualize the device configuration. Figure 4(a) shows scanning photocurrent maps of the BP FET at different set of (V_{ds}, V_g), where the black dashed lines indicate the underlying graphene source and drain electrodes, the black full line denotes the graphene top-gate electrode, and the white dashed line represents the BP film. We chose the 532-nm laser for photoelectric measurements, because the 532-nm laser is visible in both microscope and visible-light CCD, which is convenient to determine the measuring location of the devices. During the scanning, a laser with the spot diameter of ∼ 3 μm is focused on the device, whose wavelength and power are 532 nm and 25 μW, respectively. The current flowing from left to right are defined as positive. Then we observe nine different visual maps with photocurrent in the color scale, as shown in Fig. 4(a). It is noted that the photocurrent mainly comes from the contact regions between BP and the graphene, which implies that band bending happens at the contacts. Nine photocurrent maps are distinguished from each other by the different photocurrent distribution of the contacts.

To explain the photocurrent maps, we draw the simplified band diagram according to the analysis in Fig. 3, as displayed in Fig. 4(b). In equilibrium state, *i.e.*, (0 V, 0 V), few nanoamperes of the photocurrent is observed, which is almost 2 orders less than the current of other nonequilibrium configurations.

The reason for this weak photoresponse is because the band bending in this slight p-type configuration is not strong enough to boost the electron–hole separation and finally leads to negligible photocurrent. Generally, the sign of the photocurrent is determined by the slope of the band bending. Taking the case of (−2 V, −1 V) as an example, as shown at the top middle map in Fig. 4(a), negative photocurrents at both contacts are measured, consistent with the n–i–p configuration at the top middle diagram shown in Fig. 4(b). For the one junction case such as the p–i configuration (2 V, 0 V), only a positive photocurrent at the left contact is observed, as shown at the bottom left map in Fig. 4(a), corresponding to a flat-band configuration near the right contact. For the overall p- or n-dominant configurations in the middle left or right diagram shown in Fig. 4(b), we measure the photocurrents with opposite directions at each contact shown in Fig. 4(a). In a word, all nine configurations with the band diagram shown in Fig. 4(b) match the SPCM images shown in Fig. 4(a) very well.

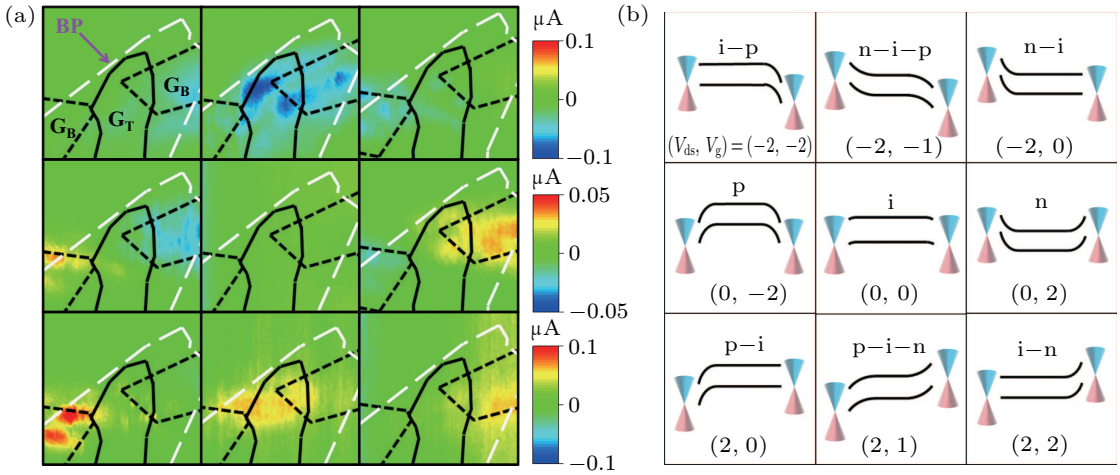


Fig. 4. (color online) Reconfigurable SPCM with band diagrams. (a) SPCM maps of the BP FET with color scale for nine different configurations. The sets of (V_{ds}, V_g) for each configuration in turn are: (−2 V, −2 V), (−2 V, −1 V), (−2 V, 0 V), (0 V, −2 V), (0 V, 0 V), (0 V, 2 V), (2 V, 0 V), (2 V, 1 V), and (2 V, 2 V), respectively. (b) The corresponding schematic band diagrams of SPCM maps.

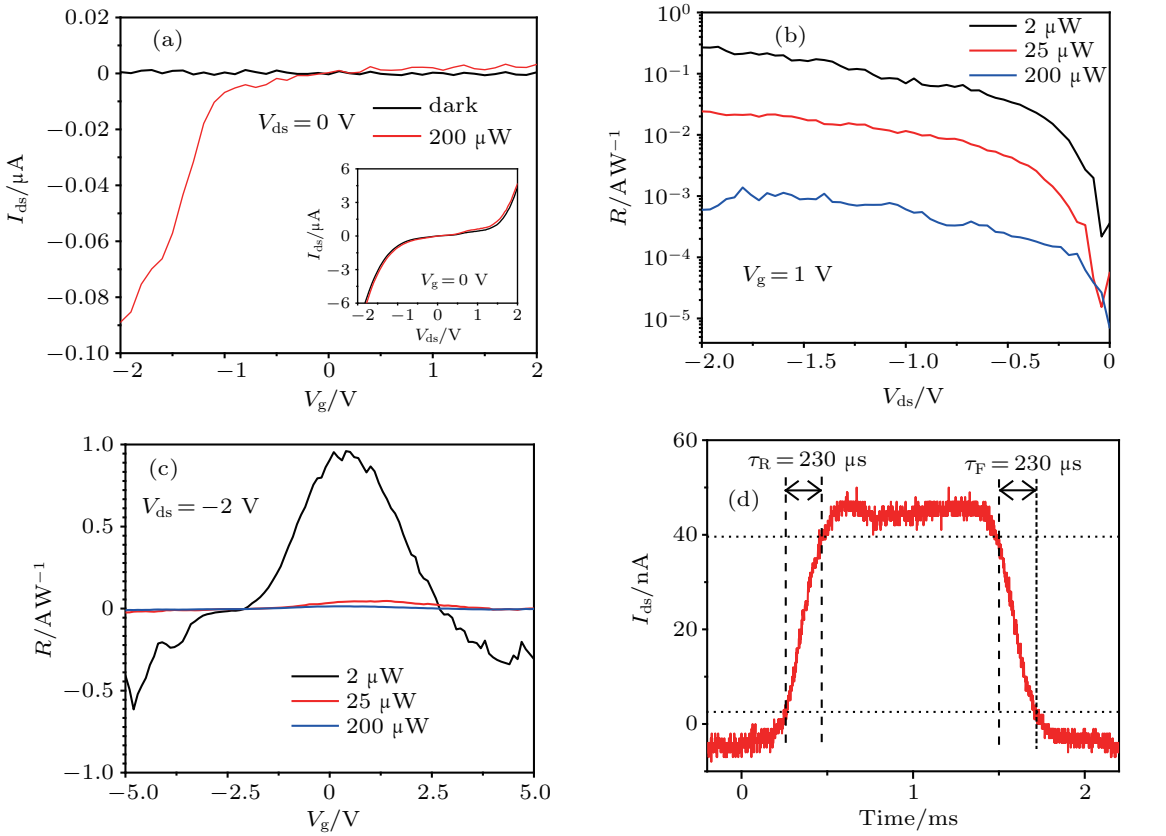


Fig. 5. (color online) Photocurrent measurements of the phototransistor with a 532-nm laser illuminated at one BP-graphene contact region. (a) I_{ds} with respect to V_g at $V_{ds} = 0$ V in dark (black line) and illumination (red line) at the contact region. The laser power is 200 μW. Inset: I_{ds} versus V_{ds} curves at $V_g = 0$ V. (b) The responsivity R versus V_{ds} curves when $V_g = 1$ V and (c) R versus V_g curves when $V_{ds} = -2$ V with three different laser powers (black: 2 μW, red: 25 μW, blue: 200 μW). (d) Time response measurement of I_{ds} by using a chopper.

To investigate the photoresponse of our BP-based transistor, photocurrent measurements are carried out at a BP-graphene contact. Figure 5(a) shows I_{ds} versus V_g curves at $V_{ds} = 0$ V (inset: I_{ds} versus V_{ds} curves at $V_g = 0$ V) in dark (black line) and under 200-μW laser illumination (red line). An obvious photoresponse is observed except $V_g = V_{ds} = 0$ V. The negligible photoresponse at $V_g = V_{ds} = 0$ V directly proves the i-type assumption presented in Fig. 3(a). The responsivity (R) is defined as the photocurrent generated per unit power of incident light,[9]

$$R = I_{ph}/P, \tag{2}$$

where the photocurrent $I_{ph} = I_{illum} - I_{dark}$ and the light intensity P is the laser power due to the small laser spot. From the results of Figs. 5(b)–5(c), it is found higher responsivity can be obtained for weaker laser, and a high R up to 800 mA/W is measured at the low power of 2 μW when $V_{ds} = -2$ V and $V_g = 1$ V, which dramatically decreases to 0.6 mA/W at 200 μW. The presence of the trap states either in BP or at the interface between BP and other 2D material layers may be responsible for such a reduction in photoresponsivity.[24] This nonlinear response of R is also reported in many 2D or heterostructure devices.[25–30] Hence, the poor linear dynamic range needs to be improved for further photodetector application. The external quantum efficiency EQE is estimated as $(I_{ph}/P)/(hc/e\lambda) = 37.7\%$ at the high value of R, where h and c are Planck's constant and the speed of light, respectively. In addition, the time response of photocurrent with a chopper is recorded for the p–i configuration ($V_{ds} = 2$ V, $V_g = 0$ V), as shown in Fig. 5(d), from which one can find the rise time τ_R and the fall time τ_F are both evaluated as 230 μs.

4. Summary

In summary, we have fabricated a van der Waals heterostructured top-gate transistor with all 2D constituents (including BP, graphene, and h-BN layers). By applying less than 2 V of both top-gate and source–drain voltages, this device has been reconfigured successfully by utilizing the ambipolar tunable characteristics of BP channel, where nine different configurations have been realized. By spatially resolved scanning photocurrent microscopy technique, all configurations were directly visualized, and the photocurrent was only detected at the contact regions where band bending occurred. In addition, high responsivity and fast photoresponse speed have been observed in the devices, assuring the potential ability in photodetection. Consequently, our reconfigurable heterostructured BP transistors may offer a potential useful structure towards electrically tunable photovoltaic devices.

Acknowledgment

We thank the AFM measurements by the Analytical and Testing Center of Northwestern Polytechnical University.

References

[1] Novoselov K S, Geim A K, Morozov S V, Jiang D, Katsnelson M I, Grigorieva I V, Dubonos S V and Firsov A A 2005 *Nature* **438** 197
[2] Zhang Y, Tan Y W, Stormer H L and Kim P 2005 *Nature* **438** 201
[3] Novoselov K S, Jiang D, Schedin F, Booth T J, Khotkevich V V, Morozov S V and Geim A K 2005 *Proc. Natl. Acad. Sci. USA* **102** 10451
[4] Dean C R, Young A, Meric I, Lee C, Wang L, Sorgenfrei S, Watanabe K, Taniguchi T, Kim P, Shepard K L and Hone J 2010 *Nat. Nanotechnol.* **5** 722
[5] Radisavljevic B, Radenovic A, Brivio J, Giacometti V and Kis A 2011 *Nat. Nanotechnol.* **6** 147
[6] Ross J, Klement P, Jones A M, Ghimire N, Yan J, Mandrus D, Taniguchi T, Watanable K, Kitamura K, Yao W, Cobden D and Xu X 2014 *Nat. Nanotechnol.* **9** 268
[7] Kim K, Choi J, Kim T, Cho S and Chung H 2011 *Nature* **479** 338
[8] Novoselov K S, Fai Ko V I, Colombo L, Gellert P R, Schwab M G and Kim K 2012 *Nature* **490** 192
[9] Koppens F H L, Mueller T, Avouris Ph, Ferrari A C, Vitiello M S and Polini M 2014 *Nat. Nanotechnol.* **9** 780
[10] Xia F, Wang H and Jia Y 2014 *Nat. Commun.* **5** 4458
[11] Liu H, Neal A T, Zhu Z, Luo Z, Xu X, Tomanek D and Ye P D 2014 *ACS Nano* **8** 4033
[12] Li L, Yu Y, Ye G J, Ge Q Q, Ou X, Wu H Feng D L, Chen X and Zhang Y 2014 *Nat. Nanotechnol.* **9** 372
[13] Qiao J, Kong X, Hu Z, Yang F and Ji W 2014 *Nat. Commun.* **5** 4475
[14] Koenig S P, Doganov R A, Schmidt H, Castro Neto A H and Özyilmaz B 2014 *Appl. Phys. Lett.* **104** 103106
[15] Buscema M, Groenendijk D J, Blanter S I, Steele G A, Van Der Zant H S J and Castellanosgomez A 2014 *Nano Lett.* **14** 3347
[16] Dai J and Zeng X C 2014 *J. Phys. Chem. Lett.* **5** 1289
[17] Tran V, Soklaski R, Liang Y and Yang L 2014 *Phys. Rev. B* **89** 235319
[18] Chen X, Wu Y, Wu Z, Han Y, Xu S, Wang L, Ye W, Han T, He Y, Cai Y and Wang N 2015 *Nat. Commun.* **6** 7315
[19] Wang L, Meric I, Huang P Y, Gao Q, Gao Y, Tran H, Taniguchi T, Watanabe K, Campos L M, Muller D A, Guo J, Kim P, Hone J, Shepard K L and Dean C 2013 *Science* **342** 614
[20] Castellanosgomez A, Buscema M, Molenaar R, Singh V, Janssen L, Van Der Zant H S J and Steele G A 2014 *2D Mater.* **1** 011002
[21] Saito Y, Iwasa Y 2015 *ACS Nano* **9** 3192
[22] Warschauer D M 1963 *J. Appl. Phys.* **34** 1853
[23] Li D, Wang X, Zhang Q, Zou L, Xu X and Zhang Z 2015 *Adv. Funct. Mater.* **25** 7360
[24] Kind H, Yan H, Messer B, Law M and Yang P 2002 *Adv. Mater.* **14** 158
[25] Lopezsanchez O, Lembke D, Kayci M, Radenovic A and Kis A 2013 *Nat. Nanotechnol.* **8** 497
[26] Chen Y, Wang X, Wu G, Wang Z, Fang H, Lin T, Sun S, Shen H, Hu W, Wang J, Sun J, Meng X and Chu J 2018 *Small* **14** 1703293
[27] Liu F, Shimotani H, Shang H, Kanagasekaran T, Zolyomi V, Drummond N, Fal Ko V I and Tanigaki K 2013 *ACS Nano* **8** 752
[28] Zhang E, Jin Y, Yuan X, Wang W, Zhang C, Tang L, Lou S, Zhou P, Hu W and Xiu F 2015 *Adv. Funct. Mater.* **25** 4076
[29] Wang X, Wang P, Wang J, Hu W, Zhou X, Guo N, Huang H, Sun S, Shen H, Lin T, Tang M, Liao L, Jiang A Q, Sun J, Meng X, Chen X, Lu W and Chu J 2015 *Adv. Mater.* **27** 6575
[30] Mudd G W, Svatek S A, Hague L, Makarovsky O, Kudrynskyi Z R, Mellor C J, Beton P H, Eaves L, Novoselov K S, Kovalyuk Z D, Vdocin E E, Marsden A J, Wilson Neil R and Patane A 2015 *Adv. Mater.* **27** 3760